Impact of metal artifacts due to EEG electrodes in brain PET imaging

Catherine Lemmens, Marie-Louise Montandon, Johan Nuyts, Osman Ratib and Habib Zaidi

***Abstract*— Neurological PET/CT examinations are often performed with electroencephalogram (EEG) monitoring for epilepsy patients. However, the EEG electrodes cause metal artifacts in the reconstructed CT images which might propagate through the attenuation map into the PET reconstructions. In this study, the impact of the electrodes on the visual quality and quantification of brain PET images was investigated. Methods: Twenty epilepsy patients with EEG monitoring referred for a PET/CT examination were used. The CT data were reconstructed using both FBP yielding an artifactual image and a metal artifact reduction (MAR) algorithm yielding a CT image with reduced artifacts. Both data sets were used for CT-based attenuation correction (AC) of the PET data. In addition, a calculated attenuation correction (CALC) technique using a three-compartment model (brain tissue, skull and scalp) was also considered. This resulted in three PET reconstructions for each patient which were assessed visually and analyzed quantitatively. For the quantitative analysis, the PET images were spatially normalized to a 3D 18F-FDG stereotactic template. The mean activity concentration of 63 VOIs was calculated for each PET image and correlations between the different AC methods were assessed on a VOI by VOI basis using MAR-based AC as the gold standard. The visual assessment showed local hot spots corresponding to the locations of the electrodes when using FBP-AC. These artifacts disappeared when MAR-AC or CALC-AC were used. However, the tracer uptake was overestimated in the neighborhood of the nasal cavities when using with the CALC-AC. The quantitative analysis showed a very good correlation (R^2=0.99) between FBP-AC and MAR-AC, however a bias ranging from 4.1% to 5.4% was noticed. There was also a good correlation between CALC-AC and MAR-AC (R^2=0.98) with a bias ranging from -5.1% to 4.3%. The EEG electrodes give rise to local hot spots and quantification bias. The use of the MAR algorithm combined with an optimized attenuation coefficient for the electrodes significantly reduces the artifacts and bias. When a CT scan is not available, the use of a three-compartment calculated attenuation map is a good alternative; however care has to be taken in the neighborhood of air and nasal cavities.**

Keywords: PET/CT, brain imaging, attenuation correction, metal artifacts, quantification.

I. Introduction

During the last decade, Positron Emission Tomography (PET) has worked its way into daily clinical routine. PET has become the imaging modality of choice for diagnosis, staging and restaging, and follow-up in oncology. In neurology, the importance of PET is still growing and steadily gaining importance both in clinical and research settings. Brain PET imaging enables in vivo visualization of cerebral blood flow, brain metabolism and neuroreceptor bindings. To obtain quantitative PET images, the acquired projection data have to be corrected for photon attenuation which has long been recognized as the most important physical degrading factor resulting in the loss of quantification ability [1]. In standalone PET, patient-specific attenuation correction factors (ACF) are usually obtained by acquiring a transmission scan using external positron-emitting (^{68}Ga/^{68}Ge) or single-photon (^{137}Cs) emitting radionuclide sources. Transmission scanning increases the total examination time considerably and produces a noisy attenuation map. In brain PET imaging, one can make use of alternative methods to obtain the attenuation map including calculated [2], [3] and atlas-guided [4], [5], [6] methods. Numerous publications reported on the comparative assessment of a variety of attenuation correction strategies in brain PET imaging [1]. In particular, a comparative study involving six different attenuation correction algorithms using clinical data revealed significant differences between the different attenuation techniques [6]. With the advent of combined PET/CT, the CT images are used for attenuation correction of the PET data. This eliminates the need for a lengthy transmission scan and results in an attenuation map with reduced noise. However, in the presence of high density material, like metals and concentrated oral contrast, the CT images contain streak artifacts. These artifacts may propagate into the PET images during the CT-based attenuation correction procedure thus disturbing the visual interpretation and influencing the quantitative analysis [7], [8], [9]. Metal artifact reduction (MAR) algorithms have been developed to reduce the artifacts in the CT images [10] [11] [12], thereby restoring the tracer concentration in the PET images. In neurological PET/CT, epilepsy patients often get electroencephalogram (EEG) monitoring during their examination. However, the metal EEG electrodes will cause artifacts in the CT images and thereby affect the PET images. In this study, the impact of the electrodes on the visual quality and the quantification of brain PET images is investigated. To this end, PET images corrected for attenuation using the artifactual CT images are compared to PET images corrected for attenuation using CT images corrected for metal artifacts. In addition, a comparison is also made with an automated calculated attenuation correction technique using a three-compartment model (brain tissue, skull and scalp). This procedure might be useful if the CT part of PET/CT is in breakdown regime or in many other situations

C. Lemmens and J. Nuyts are with the Dept. of Nuclear Medicine, K.U.Leuven, Leuven, Belgium, (e-mail: catherine.lemmens@uz.kuleuven.be). M-L. Montandon, O. Ratib and H. Zaidi are with the Dept. of Nuclear Medicine, Geneva University Hospital, Switzerland. This work was supported by the "Institute for the Promotion of Innovation through Science and Technology in Flanders (IWT-Vlaanderen)" and by the Swiss National Science Foundation under grant SNSF 3100A0-116547.

where radiation dose is a concern.

II. Method

A. Patient Data Acquisition

The study population consisted of 20 patients with EEG monitoring referred to the Nuclear Medicine Division of Geneva University Hospital for detection of epileptic foci with seizures using [^{18}F]-Fluorodeoxyglucose (FDG). Their age ranged from 6 to 61 years (meanSD = 26.1014.76). The EEG Genuine Grass Precious Metal Electrodes used in this study were supplied by Astro-Med, Inc. (West Warwick, RI, USA). PET/CT data acquisition was performed on a Biograph Sensation 16 (Siemens Medical Solutions, Erlangen, Germany) using a standard protocol recommended by the manufacturer. The PET acquisition was started approximately 30 min after injection of 370 MBq of [^{18}F]-FDG. The PET emission study (20 min, 1 bed position) followed immediately the CT study used for attenuation correction. Diagnostic quality CT imaging was performed under standard conditions (140 kVp, 320 mAs, 16x0.75 collimation, a pitch of 0.8 and 1.5 sec per rotation). All data required for reconstruction and creation of CT-based attenuation maps (PET sinograms, normalization file and raw CT data sets) were transferred through the hospital network to another computer for offline processing to free the PET/CT scanner for clinical usage.

B. Phantom Data Acquisition

On clinical CT scanners, the maximum CT number in the CT images is 3071 Hounsfield units (HU) except when an extended CT scale is used [13]. This means all metallic objects will be set to 3071 HU, which underestimates their true HU. Even when the extended CT scale would be used, the current conversion methods would probably result in incorrect PET attenuation values for metallic objects. If these CT images are used for attenuation correction of the PET images, lines of response (LORs) passing through metallic objects will be wrongly corrected. Therefore, a phantom experiment was conducted in order to estimate the effective attenuation coefficient of the electrodes at 511 keV. A uniform cylindrical phantom (22 cm diameter) containing ^{68}Ge/^{68}Ga to which eight EEG electrodes were attached on a single plane was used. A CT scan (140 kVp, 140 mAs, 16x0.75 collimation, a pitch of 0.8 and 0.75 sec per rotation) and PET scan (1 bed position of 30 min) were acquired on the same PET/CT system described above. Raw CT and PET data were exported for offline reconstruction (see section "Reconstruction of CT and PET data"). A transaxial slice of the reconstructed PET images, unaffected by the electrodes, was selected to serve as the reference slice. The optimal attenuation coefficient of the electrodes at 511 keV was defined as the value for which the sum of squared differences between the artifactual slice with electrodes and the reference slice was minimized.

C. Simulation studies

Two computer simulation studies were performed. The first simulation reproduced the phantom experiment described above and was performed to confirm the results obtained in the physical experiment. The second simulation study was performed to validate the reconstruction procedure described in the following section. For this purpose, one transaxial CT and brain PET image set of a patient without EEG monitoring was selected from the database. Using these clinical data as input, CT and PET projection data were generated using analytical simulators and afterwards reconstructed. Then a second simulation was performed by adding six electrodes to the CT reference image (PET-REF) and again CT and PET images were reconstructed using the second data set. Figure 1A shows the reference CT image with the six electrodes whereas the reference PET activity distribution is shown in figure 1D.

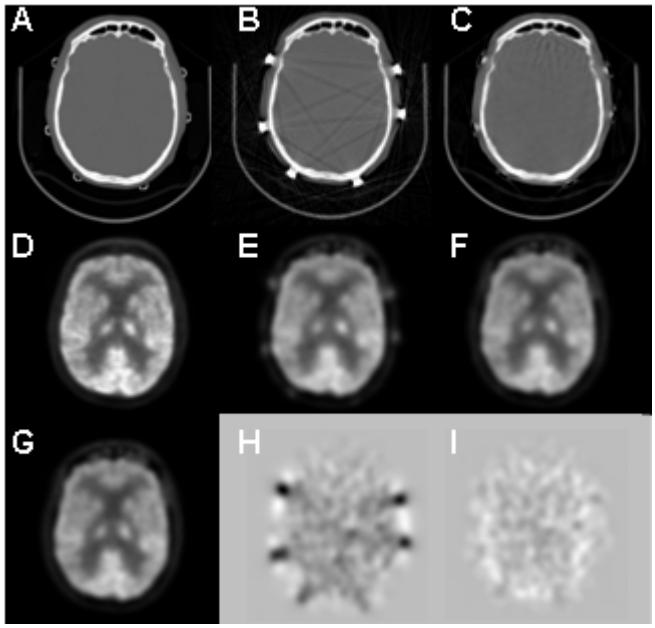

Fig. 1. Reconstructions from the simulation study. The top row shows the CT images and the middle row shows the corresponding PET images. A) The CT reference image with electrodes, B) the CT FBP reconstruction, C) the CT MAR reconstruction with the electrodes set to zero attenuation, D) the reference PET image, E) PET-FBP-AC, F) PET-MAR-AC, G) the PET reconstruction of the simulation without the electrodes (PET-REF), H) the difference image of PET-REF and PET-FBP-AC, and I) the difference image of PET-REF and PET-MAR-AC.

D. Reconstruction of CT and PET data

The CT data were rebinned from 3D cone beam into 2D parallel beam configuration and then reconstructed twice at PET resolution (336x336 pixels). The first CT reconstruction was performed using conventional filtered back projection (FBP), which gave rise to typical artifactual images owing to presence of metals in the field of view. The second reconstruction used the MAR algorithm described in [12]. The algorithm starts with an initial reconstruction performed with a Maximum-Likelihood algorithm for Transmission tomography (MLTR) [14]. Based on this initial reconstruction, a label image is created on which multi-modal priors [15], [16] are defined.

Using these priors a Maximum-A-Posteriori (MAP) [17] reconstruction is performed in order to obtain an artifact-free starting image. This starting image is the basis for an image-based projection completion procedure in which the original metal projections are replaced by artificial projections. In the last step of the algorithm, the final reconstruction is obtained by using the corrected dataset and MLTR. Figure 2 shows the result of applying the MAR algorithm to CT data of a patient having multiple dental fillings. The metal pixels

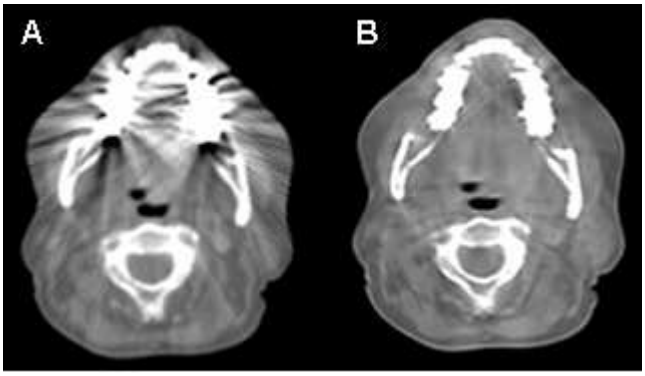

Fig. 2. CT image of a patient with multiple metallic dental fillings showing A) The FBP reconstruction, and B) the MAR reconstruction. Note the substantial reduction of artifacts when using MAR thus improving the diagnostic quality of the CT images.

in the MAR CT images are assigned appropriate attenuation coefficients based on the results of the phantom experiment described above. After reconstruction, the CT images were visually compared for spatial alignment with the PET images reconstructed without attenuation correction (PET-NOAC). In the case of visual mismatch between the two sets, the CT image is rigidly registered to the PET-NOAC using an automated mutual information-based registration procedure to compensate for patient movement between the two scans. Before conversion to attenuation maps, the CT images were Gaussian smoothed using a full width at half maximum (FWHM) of 7 mm. The conversion was performed using a bilinear tube voltage-dependent scaling method [18]. For the calculated attenuation map, the contour of the head was automatically derived from the emission sinogram using a method described in [19]. The method starts by low pass filtering the sinogram and setting all pixels having an intensity below a (very small) threshold to 1. This sinogram is backprojected to produce an image that contains for every pixel the fraction of projection lines with (nearly) zero count. A threshold of 0.1 is applied to this image to generate the head contour. This method is efficient if most projection lines intersecting the head contour yielded a count rate significantly higher than zero. Based on our experience, the technique is robust and reliable for 18F-FDG brain imaging. A skull with a fixed thickness of 5 mm was added at a depth of 10 mm from the external contour of the head. The attenuation coefficients at 511 keV used for brain (and scalp) tissue and skull were calculated using photon cross section data from the XCOM library [20] resulting in values of 0.099 cm-1 and 0.151 cm-1, respectively. The attenuation of the head holder was taken into account by manually delineating the head holder in the CT images and repositioning it into the calculated attenuation map after appropriate scaling to 511 keV. The 3D PET sinograms were corrected for detector sensitivity, dead time, scatter [21] and attenuation, and converted to 2D sinograms using Fourier rebinning [22]. For reconstruction, the sinograms were ”uncorrected” for attenuation, and reconstructed with (attenuation weighted) Maximum-Likelihood Expectation Maximization (MLEM), accelerated using a gradually decreasing number of subsets [23]. The resolution of the PET images was further enhanced by incorporating a spatially invariant point spread function in the projector (5 mm FWHM) which also reduced the noise in the images [24]. For each patient, three PET attenuation corrected images were obtained (figure 3): one PET image corrected with the CT-FBP reconstruction (PET-FBP-AC), PET corrected with the CT-MAR reconstruction (PET-MAR-AC) and PET corrected with the calculated attenuation (PET-CALC-AC).

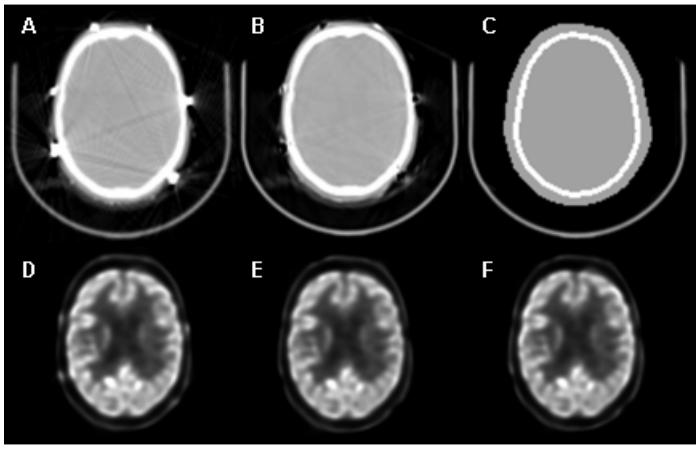

Fig. 3. The top row shows a transaxial slice of the attenuation correction maps while the bottom row shows the corresponding reconstructed PET images. A) CT FBP reconstruction, B) CT MAR reconstruction, C) the calculated attenuation map, D) PET-FBP-AC, E) PET-MAR-AC, and F) PET-CALC-AC.

E. Qualitative and Quantitative Image Analysis

Qualitative image assessment was performed by two independent observers (experienced nuclear medicine physicians) that blindly assessed visually the images reconstructed using the three different protocols. Transaxial, sagittal and coronal slices were displayed without any identification beside a code not known by the 2 observers involved in the evaluation. Each observer was asked to assess overall image quality and instructed to indicate any visible artifacts or unexpected abnormalities that could be attributed to unsatisfactory reconstruction. Reconstructed PET images using the three attenuation correction methods (PET-FBP-AC, PET-MAR-AC, and PET-CALC-AC) were also quantitatively analyzed using the latest version of BRASS automated functional brain analysis software (Hermes BRASS software, Nuclear Diagnostics AB, Sweden) which

incorporates an option allowing to perform image coregistration with warping to the stereotactic template. This technique was found to produce the least mis-warping to template induced by abnormalities, and performed consistently better than other available methods for the above experiments. Briefly, BRASS fits and compares patient images to 3-D reference templates created from images of healthy subjects [25]. The three PET attenuation corrected images were registered individually to the BRASS template for automated volume of interest (VOI)-based and voxel-based analysis of whole-brain data quantitative analysis. The ^{18}F-[FDG] standardized brain template used in this work was built by averaging 12 PET images of normal subjects in a fasting state with eyes open, ears plugged, and in a moderately lit environment. The region map consists of a total of 63 defined regions. The cost or optimization function used during automatic fitting to determine the similarity of the coregistered image to the template is based on normalized mutual information criterion which is similar to mutual information but is usually more robust and efficient in finding the correct fitting transform [26]. The voxel-based analysis compares the activity in the patient studies voxel by voxel with the activity in the normal template following count value normalization by the ratio of the total counts over the whole VOI set. Voxels located outside the global VOI region map are masked. The technique uses a region-growing algorithm where the extent of the quantitative metabolic defect is delineated by adding together the number of profile points falling below the normal limit of counts inside the region map defined on the template. The correlation between mean activity concentration estimates obtained when using the three attenuation correction methods was checked on a VOI by VOI basis and using pooled VOI analysis. The means, standard errors and standard deviations of activity concentration estimates from clinical PET images reconstructed using the three attenuation correction techniques were compared. The relative difference was used as a figure of merit for comparative assessment both within subject and as group consisting of a homogenous population.

III. Results

A. Phantom and Simulation Studies

The phantom experiment was conducted to derive the effective PET attenuation coefficient to be used for the electrodes which was defined as the value for which the sum of squared differences between the artifactual slice containing the electrodes and the reference slice was minimized. The optimal value to use for the attenuation of the electrodes turned out to be zero. In addition, the standard deviation for a large region of interest [27] in the artifactual slice was calculated. Yet again, a zero attenuation value gave the minimum standard deviation. The experimental phantom measurement was also repeated in a simulation study which confirmed that the optimal attenuation value is zero. Figure 1 shows the reconstructions of the second simulation study performed to validate the reconstruction procedure. Consistent with the experimental measurements, this simulation study also demonstrated that a zero PET attenuation value for the electrodes minimizes the sum of square differences between PET-REF and PET-MAR-AC. Figure 1 shows that MAR allows to reduce significantly the streaks due to the metallic electrodes; however the MAR reconstructed image is not artifact-free. The qualitative visual assessment showed that the PET-FBP-AC image suffers from artifacts corresponding to the location of the electrodes. These artifacts disappear in the PET-MAR-AC image. The difference images revealed that the extent of the artifacts is not confined to the location of the electrodes as the tracer uptake is overestimated with PET-FBP-AC over the whole brain. The tracer uptake is slightly underestimated in the neighborhood of the skull when using PET-MAR-AC; however the difference within the brain structures is negligible.

B. Qualitative Visual Assessment

There was excellent concordance between both observers in terms of reporting the appearance of hot-spot artifacts in the FBP-CT attenuation corrected PET images resulting from overcorrection of dense metallic electrodes. As a rule of thumb, examination of the uncorrected images in clinical routine was recommended to distinguish technical artifacts from physiologic/pathologic abnormalities. These artifacts disappeared completely when using MAR-CT for attenuation correction. Figure 4(A-D) illustrates the spatial correlation between the location and number of electrodes in the CT data and difference in tracer quantification between PET-MAR-AC and PET-FBP-AC reconstructions. For the case shown in this example, a 12% difference between the two reconstructions for the VOI corresponding to the right gyrus supramarginalis (RGS) was reported. Likewise, the PET-CALC-AC reconstructions successfully eliminated the visible hot-spot artifacts. However, invalid assumption of tissue uniformity by CALC-AC might lead to appearance of visible artifacts and significant activity quantitation bias in some regions [6]. Neglecting the non-uniform characteristics of the attenuation map in regions of high variability, such as air cavities and nasal sinuses, was observed to overestimate the tracer uptake in neighboring tissues as a result of overestimation of attenuation in these regions (figure 4(E-H)).

C. Quantitative Analysis

The slopes and correlation coefficients between mean activity concentration estimates obtained when using the three attenuation correction techniques where MAR-AC serves as gold standard are shown in figure **??**. Also shown is the linear regression plot for all VOIs from all patients. It can be seen from this figure that PET-MAR-AC and PET-FBP-AC correlate very well and that the slopes of the regression lines are close to the line of identity. PET-MAR-AC and PET-CALC-AC correlate well but a greater variation of the slope values can be observed. This variation is also noted in the Box and Whisker plots shown in figure 6. The mean relative differences between MAR-AC and CALC-AC per patient vary between -5.1% and 4.3%, whereas the range is limited to 4.1-5.4% for MAR-AC

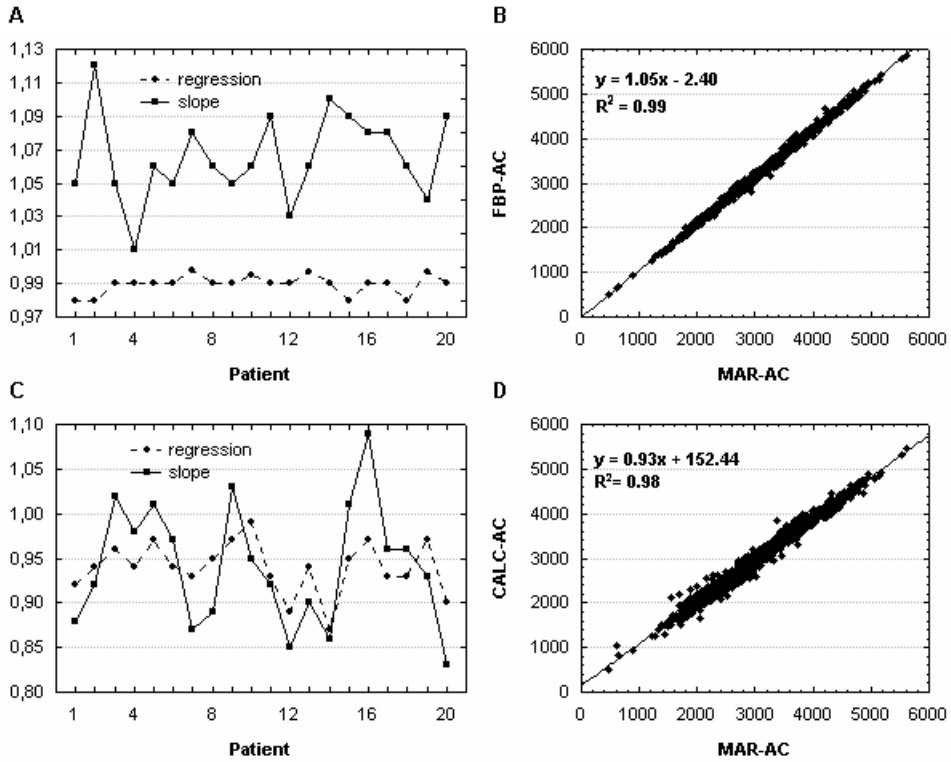

Fig. 5. Plots of correlation coefficients (R2) and slopes for each patient resulting from the linear regression analysis between A) PET-FBP-AC and PET-MAR-AC and C) PET-CALC-AC and PET-MAR-AC. The linear regression plots of all VOIs from all patients show the correlation between B) PET-FBP-AC and PET-MAR-AC and D) PET-CALC-AC and PET-MAR-AC. The correlation coefficient and the best fit equation are also shown.

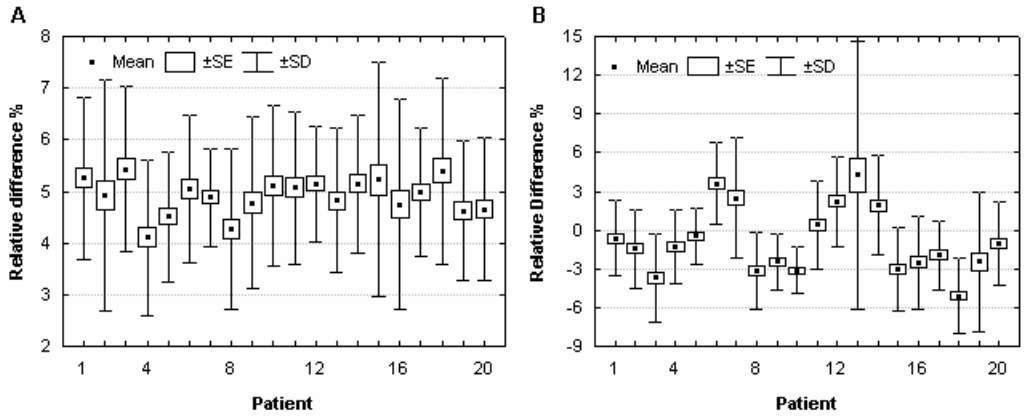

Fig. 6. Box and Whisker plots showing relative differences between reconstructions obtained by using A) MAR-AC and FBP-AC and B) MAR-AC and CALC-AC. Means, standard errors as well as standard deviations are calculated over all VOIs for each of the 20 patients studied.

and FBP-AC. Figure 7 shows the mean relative differences between the different attenuation correction methods over all patients for each VOI. The high standard deviations for the right and left gyrus orbitalis (RGO and LGO) is the result of a relatively high relative difference between PET-MAR-AC and PET-FBP-AC for 3 patients where the uptake is moderately low in these regions thus translating to large percent differences. The mean differences between PET-MAR-AC and PET-CALC-AC vary over the VOIs with a more or less constant standard deviation except for the right and left gyrus rectus (RGR and LGR), and the right and left gyrus orbitalis (RGO and LGO). These regions show a much higher activity concentration when CALC-AC is used instead of MAR-AC. Given that these regions are in the neighborhood of the sinus cavities and since the calculated attenuation map consists of a three-compartment model comprising the brain, scalp and skull, the attenuation of the sinus cavities is overestimated (assigned attenuation coefficient of brain tissue) which results in an overestimation

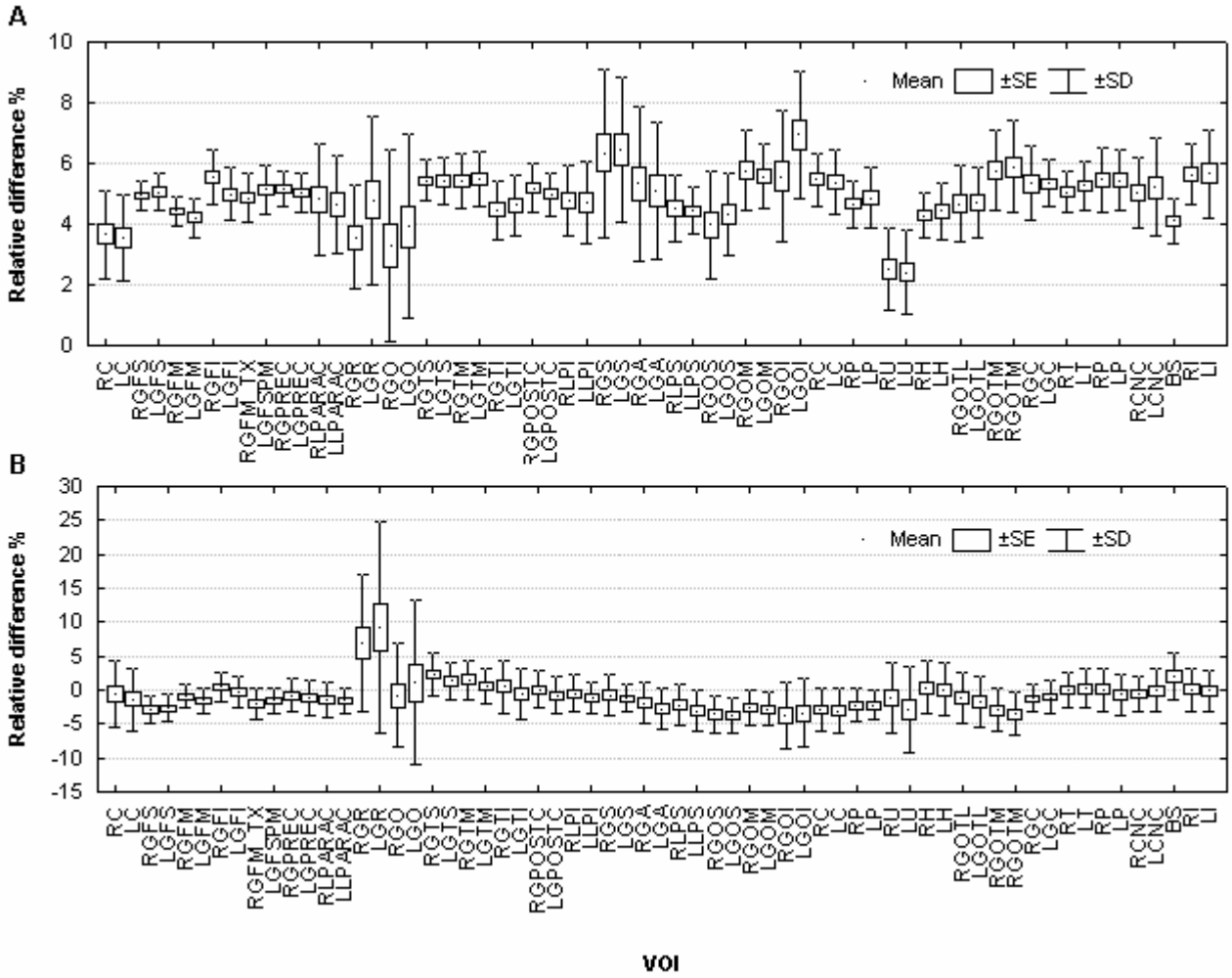

Fig. 7. Box and Whisker plots showing relative differences for the 63 VOIs between reconstructions using A) MAR-AC and FBP-AC and B) MAR-AC and CALC-AC. Means, standard errors as well as standard deviations are calculated across the 20 patients studied.

of the activity concentration. This effect is exacerbated for one patient (number 13) suffering from severe left fronto-temporal complex partial seizures following hemorrhagic stroke resulting from the rupture of anterior cerebral artery aneurysm where the uptake was very low in these regions thus translating to large percent differences. In addition, the voxel-based results showed substantial changes in terms of the number, severity, size and location of hypometabolic focal defects observed by the BRASS voxel-based region-growing technique for 9 patients (45%) between PET-MAR-AC and PET-FBP-AC and 14 patients (70%) between PET-MAR-AC and PET-CALC-AC.

IV. Discussion

Current procedures for interpreting clinical brain PET in clinical diagnosis in the majority of nuclear medicine departments are still based on mere visual inspection, thereby increasing observer variance. This subjective assessment is supported in some cases by manual or automated semi-quantitative statistical image analysis techniques. Absolute quantitative estimation of physiological parameters of interest is currently restricted to research settings or institutions having access to extensive technical support. There are presently numerous quantitative statistical analysis methods described in the literature that are valuable in assisting in the interpretation of brain PET images [25], [28]. It is therefore appealing to study the impact of artifacts originating from various sources, which is the aim of this study. Except metallic dental implants, the assessment of the impact of other metallic structures on brain PET image quality and quantitative analysis has received limited attention in the literature [1]. A phantom study was conducted to investigate whether deep brain stimulation metallic leads can create visual and/or quantifiable artifacts in neurological PET studies [29]. The experiment showed the absence of visible artifacts owing to the small size of the metallic leads. In the patient study described in this paper, the impact of EEG electrodes on the visual quality and the quantification of PET images was investigated. The presence of EEG electrodes was shown to produce local hot-spot artifacts in CT-based attenuation corrected images thus

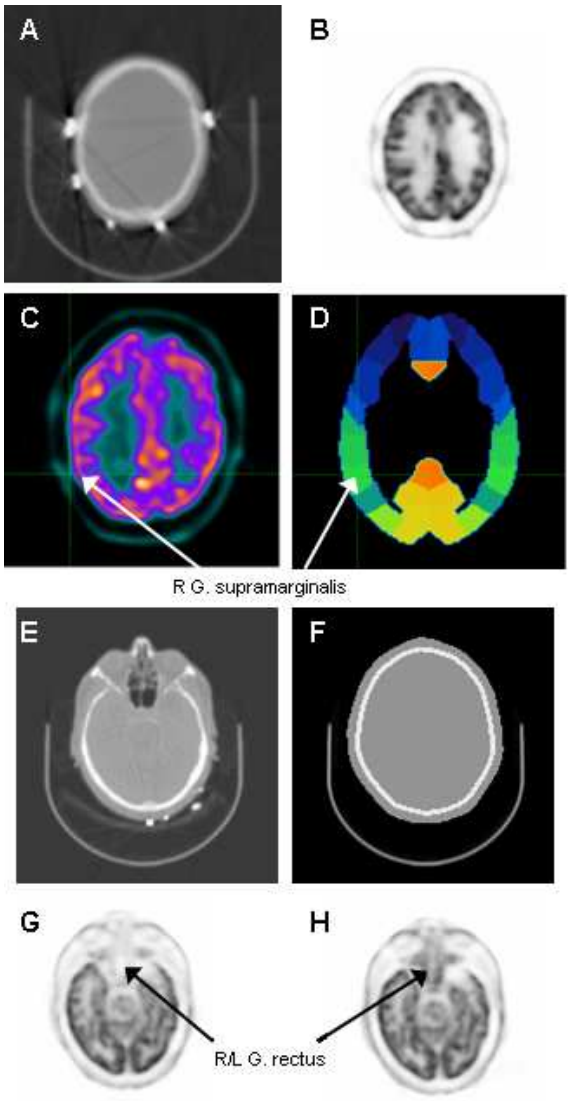

Fig. 4. The two top rows illustrate the spatial correlation between the location and number of electrodes in the CT data and difference in tracer quantification between MAR and FBP PET reconstructions. A) CT-FBP, B) PET-FBP-AC, C) the PET image coregistered to the template, and D) corresponding region map defined on the template. The arrows indicate the right gyrus supramarginalis VOI which is correlated with the locations of the electrodes and related artifacts. The two bottom rows illustrate the tracer uptake overestimation in the neighborhood of the nasal cavities when using calculated attenuation correction. E) CT-FBP, F) Calculated attenuation map, G) PET-FBP-AC, and H) PET-CALC-AC. The arrow indicates the right/left gyrus rectus region.

affect the diagnostic quality and quantitative analysis of brain PET images. This is consistent with the observations made by Kamel et al (8) who studied the impact of the presence of metallic dental implants. Noticeable changes in the VOI-based and voxel-based results obtained using BRASS for quantitative analyses were observed. These changes can be subtle and difficult to detect visually or by qualitative methods. Whether these visible artifacts and quantification bias might affect the outcome of clinical diagnosis is more difficult to predict and will be the subject of future research. In the simulation study of the brain patient, the ground truth (or the exact tracer distribution) was known which allowed to compare PET-FBP-AC and PET-MAR-AC images with PET-REF. This comparison showed that the bias resulting from PET-MAR-AC was smaller than with PET-FBP-AC. Therefore it is justified to use the PET-MAR-AC as the gold standard for the comparative study. However, based on the results of the simulation study, one can expect that the bias resulting from PET-FBP-AC using clinical data underestimates the real bias. The phantom experiment where the EEG electrodes were attached on a uniform cylinder revealed that a zero attenuation value should be assigned to the electrodes in order to obtain similar activity concentration values in the artifactual slice and the reference artifact free PET slice. This zero attenuation value was rather unexpected but can be explained by two arguments: first, the electrodes are small (10 mm in diameter) and very thin. However, in the CT images they are seen as small 'blobs', so their volume is greatly overestimated when a threshold for metallic structures is used. By assigning the correct attenuation value (which is ignored - information not disclosed by the manufacturer) to the metal pixels, the real attenuation correction factors would be greatly overestimated. Second, given that these electrodes show up as blobs and due to partial volume effects in PET, some LORs will be supposed to be strongly attenuated during the reconstruction although in reality, these LORs do not pass through metallic electrodes and are not as highly attenuated as supposed. To circumvent this problem, a zero attenuation value seems adequate. One other cause for partial volume effects in PET is patients' movement between the CT and PET data acquisition. Therefore, to avoid these additional effects, the CT and PET images were visually checked for any motion. In two out of the 20 patients, motion was detected and the CT images had to be registered rigidly to the PET-NO-AC image. Motion compensation will be very important for metallic objects inside the body like dental fillings and hip prostheses because there is often a significant tracer uptake in the vicinity of these objects. Even slight movement will result in a dramatic overcorrection. CT-based attenuation correction was compared with a calculated attenuation correction method where the contour of the head was derived from the emission sinogram. Since non-uniform attenuation maps result in general in more quantitatively accurate PET images, a three-compartment model (brain tissue, skull and scalp) with a skull having a fixed thickness of 5 mm added at 10 mm depth was implemented. Additionally, the attenuation of the head holder was taken into account by manually delineating the head holder in the CT images. Ignoring the attenuation of the bed or head holder gives rise to an underestimation of activity concentration in the posterior part of the brain [30]. In this study, the head holder was manually delineated. However, as described in [1], [31], it is possible to automate the procedure using a transmission or CT scan of the head holder and the patient bed and taking into account their relative positions by reading corresponding information from the headers of the raw CT and PET projection data. The results show that the calculated attenuation method is a potential alternative to CT-based for attenuation correction

when a CT scan is not available. However, the calculated method overestimates the attenuation coefficients of the sinus and air cavities, which results in local tracer overestimation, so care has to be taken in these regions.

V. Conclusion

In neurological PET/CT, EEG electrodes give rise to local hot spots and a positive quantification bias in the PET images. However, the possible impact of these artifacts and bias on the clinical outcome of patients' diagnosis still need further investigation. It was also shown in this study that the use of a MAR algorithm in combination with an optimal attenuation value for the electrodes allows to reduce artifacts and bias in the brain images. Whether it would be opportune to use MAR in combination with an optimal attenuation value for other kinds of metal artifacts is also a subject for further investigation. When a CT scan is not available, it was shown that the use of a three-compartment calculated attenuation map could be an alternative; however care has to be taken in the neighborhood of air and nasal cavities.

VI. Acknowledgements

The authors thank David Faul, James Hamill, Krank Kehren and Christian Michel from Siemens Medical Solutions, MI, Knoxville, USA for advice and software.

References

[1] Zaidi H, Montandon M-L, Meikle S. Strategies for attenuation compensation in neurological PET studies. Neuroimage 2007;34:518-541.

[2] Siegel S, Dahlbom M. Implementation and evaluation of a calculated attenuation correction for PET. I EEE Trans Nucl Sci. 1992;39:1117-1121.

[3] Weinzapfel BT, Hutchins GD. Automated PET attenuation correction model for functional brain imaging. J Nucl Med. 2001;42:483-491.

[4] Stodilka RZ, Kemp BJ, Prato FS, Kertesz A, Kuhl D, Nicholson RL. Scatter and attenuation correction for brain SPECT using attenuation distributions inferred from a head atlas. J Nucl Med. 2000;1569-1578.

[5] Montandon M-L, Zaidi H. Atlas-guided non-uniform attenuation correction in cerebral 3D PET imaging. Neuroimage 2005;25:278-286.

[6] Zaidi H, Montandon M-L, Slosman DO. Attenuation compensation in cerebral 3D PET: effect of the attenuation map on absolute and relative quantitation. Eur J Nucl Med Mol Imaging. 2004;31:52-63.

[7] Goerres GW, Ziegler SI, Burger C, Berthold T, von Schulthess GK, Buck A. Artifacts at PET and PET/CT caused by metallic hip prosthetic material. Radiology. 2003;226:577-584.

[8] Kamel EM, Burger C, Buck A, von Schulthess GK, Goerres GW. Impact of metallic dental implants on CT-based attenuation correction in a combined PET/CT scanner. Eur Radiol. 2003;13:724-728.

[9] Ay MR, Zaidi H. Assessment of errors caused by x-ray scatter and use of contrast medium when using CT-based attenuation correction in PET. Eur J Nucl Med Mol Imaging 2006;33:1301-1313.

[10] Kalender WA, Hebel R, Ebersberger J. Reduction of CT artifacts caused by metallic implants. Radiology. 1987;164:576-577.

[11] Mahnken AH, Raupach R, Wildberger JE et al. A new algorithm for metal artefact reduction in computed tomography. In vitro and in vivo evaluation after total hip replacement. Invest Radiol. 2003;38:769-775.

[12] Lemmens C, Faul D, Hamill J, Stroobants S, Nuyts J. Suppression of metal streaks artifacts in CT using a MAP reconstruction procedure. IEEE NSS-MIC 2006. Conf proc 2006; 3431-3437.

[13] Coolens C, Childs PJ. Calibration of CT Hounsfield units for radiotherapy treatment planning of patients with metallic hip prostheses: the use of the extended CT-scale. Phys Med Biol. 2003;48:1591-1603.

[14] De Man B, Nuyts J, Dupont P, Marchal G, Suetens P. Reduction of metal streak artifacts in x-ray computed tomography using a transmission maximum a posteriori algorithm, IEEE Trans Nucl Sci. 2000;47:977-981.

[15] Liang Z, Jaszczak R, Coleman R, Johnson V. Simultaneous reconstruction, segmentation, and edge enhancement of relatively piecewiece continuous images with intensity-level information. Med Phys. 1991;18:394-401.

[16] Nuyts J, Dupont P, Stroobants S, Benninck R, Mortelmans L, Suetens P. Simultaneous maximum a posteriori reconstruction of attenuation and activity distributions from emission sinograms. IEEE Trans Med Imaging. 1999;18:393-403.

[17] Qi J, Leahy RM. Iterative reconstruction techniques in emission computed tomography. Phys Med Biol. 2006;51:R541-R578.

[18] Carney JPJ, Townsend D, Rappoport V, Bendriem B. Method for transforming CT images for attenuation correction in PET/CT imaging. Med Phys. 2006;33:976-983.

[19] Ghoorun S, Baete K, Nuyts J, Groenewald W, Dupont P. The influence of attenuation correction and reconstruction techniques on the detection of hypo-perfused lesions in brain SPECT images. Nucl Med Commun 2006; 27: 765-772.

[20] Hubbel JH, Seltzer SM. Tables of X-Ray Mass Attenuation Coefficients and Mass Energy-Absorption Coefficients. NISTIR 5632. (http://physics.nist.gov/PhysRefData/XrayMassCoef/cover.html).

[21] Watson CC. New, faster, image-based scatter correction for 3D PET. IEEE Trans Nucl Sc. 2000;47:1587-1594.

[22] Defrise M, Kinahan PE, Townsend DW, Michel C, Sibomana M, Newport DF. Exact and approximate rebinning algorithms for 3-D PET data. IEEE Trans Med Imaging. 1997;16:145-158.

[23] Hudson HM, Larkin RS. Accelerated image reconstruction using ordered subsets of projection data. IEEE Trans Med Imaging. 1994;13:601-609.

[24] Zeng GL, Gullberg GT, Tsui BMW, Terry JA. Three-dimensional iterative reconstruction algorithms with attenuation and geometric point response correction. IEEE Trans Nucl Sci. 1991;38:693-701.

[25] Slomka PJ, Radau P, Hurwitz GA, Dey D. Automated three-dimensional quantification of myocardial perfusion and brain SPECT. Comput Med Imaging Graph 2001; 25:153-164.

[26] Studholme C, Hill DLG, Hawkes DJ. An overlap invariant entropy measure of 3D medical image alignment. Pattern Recogn 1999; 32:71-86.

[27] Stodilka RZ, Kemp BJ, Prato FS, Nicholson RL. Importance of bone attenuation in brain SPECT quantification, J Nucl Med 1998;39:190-197.

[28] Friston KJ, Holmes AP, Worsley KJ, Poline J-P, Frith CD, Frackowiak RSJ. Statistical parametric maps in functional imaging: a general linear approach. Hum Brain Mapp 1994;2:189-210.

[29] Ay MR, Zaidi H. Impact of X-ray tube settings and metallic leads on neurological PET imaging when using CT-based attenuation correction. Nucl Instr Meth in Phys Res A 2007;571:411-414.

[30] Bettinardi V, Gilardi MC, Cargnel S, et al. A hybrid method of attenuation correction for positron emission tomography brain studies. Eur J Nucl Med. 1994;21:1279-1284.

[31] Michel C, Bol A, De Volder AG, Goffinet AM. Online brain attenuation correction in PET: towards a fully automated data handling in a clinical environment. Eur J Nucl Med. 1989;15:712-718.